

Geometric criteria for the snap-off of a nonwetting droplet in pore-throat channels with rectangular cross-sections

Luming Cha¹, Chiyu Xie^{2,*}, Qihong Feng^{1,*}, and Matthew Balhoff^{2,3}

¹School of Petroleum Engineering, China University of Petroleum (East China), Qingdao 266580, China

²Center for Subsurface Energy and the Environment, The University of Texas at Austin, Austin, TX 78712, USA

³Hildebrand Department of Petroleum and Geosystems Engineering, The University of Texas at Austin, Austin, TX 78712, USA

Key Points:

- Geometric criteria for the snap-off in microchannels with rectangular cross-sections are proposed and classified in three categories.
- The criteria are verified by OpenFOAM simulations and validated against microfluidic experiments.
- We clarify previous debates on whether snap-off occurs in 2D microchannels and provide guidelines for the design of 2D micromodels.

Abstract

Snap-off is a phenomenon that occurs when a non-wetting fluid displaces a wetting fluid in pore-throat channels, leading to the breakup of droplets at the throat. Snap-off plays a key role in many industrial processes involving immiscible multiphase flows, such as droplet/bubble manipulation, emulsion formation, and oil recovery. Here we derive geometric criteria for the capillary snap-off at the pore-throat junctions in 2D microchannels with rectangular cross-sections. The criteria are theoretically presented in three categories according to the range of the throat depth, h . We find that if h is smaller than the throat width, snap-off will never occur, if h is larger than the pore width, snap-off may occur but it is independent of h , and if h is in between the throat width and the pore width, a critical depth exists for the occurrence of snap-off. These criteria are verified using numerical CFD simulations and validated using microfluidic experiments. These results indicate the conditions for snap-off in the pore-throat channel with rectangular cross-sections, which clarify previous debates in the literature. One application of this work is for micromodels, which are porous microfluidic chips used as tools to observe multiphase flow in porous media at the pore scale. Most micromodels are two-dimensional (2D), which have rectangular cross-sections with uniform depth. The geometric criteria derived here provide guidelines for the design of micromodels used in the study of multiphase flow processes in porous media.

Keywords: snap-off; multiphase flow; droplet generation; computational fluid dynamics; microfluidics

* Email address of corresponding author: chiyu.xie@gmail.com

* Email address of corresponding author: fengqihong@126.com

42 1. Introduction

43 The displacement of a wetting fluid by a non-wetting fluid in a pore-throat (expansion-contraction-expansion)
44 channel may result in the breakup of the non-wetting fluid into separate droplets/bubbles. This phenomenon,
45 referred to as snap-off, choke-off, or break-up (JG Roof, 1970; Ransohoff & Radke, 1989; Herring et al., 2018),
46 occurs when the capillary pressure at its leading part exceeds that at the pore-throat junction. Snap-off is an
47 important process in many industrial fields (Picchi & Battiato, 2018; Du et al., 2019; Feng et al., 2020), such as
48 enhanced oil recovery (Lenormand et al., 1983; Ransohoff et al., 1987; Mogensen & Stenby, 1998; Xu et al., 2017),
49 carbon capture and storage (Andrew et al., 2014), fuel cells (Lamanna et al., 2014), and separation processes
50 (Roman et al., 2016). The applications of porous media are a common occurrence of snap-off; however, others
51 applications, such as emulsion generation (Cunha et al., 2018), droplet/bubble manipulation (Tan et al., 2007; Xu et
52 al., 2015; Berry et al., 2019), occur in a single channel.

53 Roof (1970) proposed a quasi-static criterion for the snap-off of oil droplets in water-wet pore-throat channels
54 with circular cross-sections, in terms of the ratio between the maximum and minimum radii of the capillary tube.
55 The Roof criterion for snap-off is that the local capillary pressure at the throat is greater than the capillary pressure
56 at the pore body. This criterion has been used for decades to study snap-off behavior. Deng et al. (2014) extended
57 the Roof criterion to successional contraction-expansion channels by considering the instability of capillary
58 pressure between the pore throat and pore body. The extended criteria were successfully used to interpret the
59 simulation results of multiphase flow with supercritical CO₂ as the nonwetting phase and they proved the existence
60 of film flow downstream of the pore body. Kavscek and Radke (1996) introduced a corner-flow hydrodynamics
61 theory to predict the accumulation of the wetting fluid preceding the snap-off. Their theory focused on the pressure
62 gradients of fluid phases, which was validated by the mathematical model and micromodel experiments. It showed
63 that the pressure gradient in the wetting phase increases the tendency of liquid accumulation for snap-off.

64 Pore network models have served as an efficient and predictive tool for the simulation of flow in porous media
65 by using a network of idealized geometries to represent the complex void spaces (Valvatne & Blunt, 2004; Idowu &
66 Blunt, 2010; Tanino & Blunt, 2012; Singh et al., 2017; Xie et al., 2017; Almajid & Kavscek, 2020). The snap-off
67 criterion for pore throats in network models was proposed by Lenormand et al. (Roland Lenormand & Zarcone,
68 1984). They investigated the displacement of fluid in an etched network and found that the snap-off behavior
69 mainly depended on the portion of the non-wetting fluid in the channel. For a square throat, the threshold capillary
70 pressure for snap-off is $p_s^* = (\cos\theta - \sin\theta)\sigma/r$. This criterion was introduced into the capillary
71 equilibrium-based network models by Blunt et al. (1998). The authors proposed that the snap-off would become
72 less favored as the contact angle increased and it would be completely suppressed beyond the contact angle of 45°.
73 Nguyen et al. (2004) developed a dynamic network model for the imbibition process. They revealed that snap-off
74 is a natural consequence of film swelling, and it is related to the flow rate. Singh et al. (2019) also showed that the
75 prevalence of snap-off is a function of pore-throat geometry and wettability. However, the criteria in network
76 models are only applied to snap-off in the cross-sections of intersecting channels, which are different from the Roof
77 snap-off within a single pore-throat channel.

78 Micromodel devices are powerful tools used to directly visualize many flow and transport processes (Lifton,
79 2016; Skaue et al., 2020). Micromodels are porous microfluidic chips that are fabricated from a predetermined
80 pattern or imaged from real, naturally occurring media. Micromodels have been used to study many
81 hard-to-observe flow processes in naturally occurring porous media (Kashchiev, 2003; Kavscek et al., 2007;
82 Rossen, 2008). Due to the selectivity and anisotropy of the etching methods, the etching depth of a micromodel is
83 usually finite and uniform. As a result, micromodel devices are often two-dimensional (2D) with rectangular
84 cross-sections. Xu et al. (2017) showed that snap-off was rare in micromodels because of their 2D nature and
85 developed a “2.5D” micromodel which has varying depths throughout the model. By creating gaps between
86 neighboring pores on the mask, the authors proposed a novel fabrication approach based on the isotropic feature of

hydrofluoric (HF) acid etching. They created the 2.5D micromodel (depths of the pores and the throats are different) using this fabrication approach. 3D-printing has also been utilized to create more micromodels (Jasak et al., 2007; King, 2013) with more complex geometry and has begun to help break this barrier.

However, it is still under debate that whether or not a 2D micromodel with rectangular cross-section can cause snap-off and under what conditions. Using a 2D micromodel, Kovscek et al. (2007) observed and verified snap-off as a foam-generation mechanism in porous media. Rossen (2003) commented that the snap-off found in (Kovscek et al., 2007) was due to the regional fluctuations in capillary pressure rather than the Roof snap-off. They suggested that the 2D micromodel is problematic for snap-off investigation because of the lower coordination number and the impossibility of simultaneous two-phase flow compared with 3D structures. Moreover, the effect of channel depth on snap-off is rarely addressed. It is therefore important to determine if, and under what conditions, snap off occurs in pore-throat channels with rectangular cross-sections.

In this paper, we investigate snap-off in the pore-throat channels with rectangular cross-sections through theoretical analyses, numerical modeling, and microfluidic experiments. In Section 2, we theoretically propose three categories for the discussion of the occurrence of snap-off based on the range of the etching depth. In Section 3, numerical modeling using OpenFOAM (Jasak et al., 2007; Afsharpoor & Javadpour, 2016; Musehane & Herbst, 2019) is presented to verify the theoretical derivations. In Section 4, the validity of the criteria is further examined by the microfluidic experiments. Finally, we draw conclusions in Section 5.

2. Theoretical Analysis

The criterion for the occurrence of capillary snap-off in a pore-throat is determined by the pore-throat geometry and fluid properties, the interfacial tension σ and wettability θ . First, we revisit the derivation of the snap-off criterion for a pore-throat channel with circular cross-sections, as shown in Fig. 1a), which has been investigated by many researchers (Hirt & B.D. Nichols, 1981). Then, we derive the criterion for a pore-throat channel with a rectangular cross-section (as shown in Fig. 1b) following the same procedure.

In a water-wet pore-throat channel, Roof (1970) mathematically demonstrated that snap-off would only occur when the capillary pressure at the neck of the constriction (throat), P_{c-neck} , is larger than the capillary pressure at the droplet/bubble front, $P_{c-front}$ under low capillary number. This is because the pressure in the wetting phase is assumed to be the same everywhere (equal to $P_{c-front}$), therefore, the interface will become unstable at the throat when P_{c-neck} is equal to $P_{c-front}$. Then the wetting phase penetrates and squeezes into the center of the tube. The width of the constricted area (R_t) will then decrease, leading to a higher capillary pressure at the constriction and snap-off. Therefore, the snap-off criterion depends on the capillary pressures, P_{c-neck} and $P_{c-front}$, which can be obtained by the Young-Laplace equation.

For the pore-throat channel with circular cross-sections (Fig. 1a), capillary pressures are calculated as

$$P_{c-front} = 2\sigma / R_p \quad (1)$$

$$P_{c-neck} = \sigma \left(\frac{1}{R_t} - \frac{1}{R_o} \right) \quad (2)$$

Where R_p and R_t are the radii of principal curvatures on the y-z plane at the pore and at the throat, respectively; R_o is the radius of principal curvature at the pore on the x-y plane. When the following criterion is satisfied, capillary snap-off will occur in the pore-throat channel with circular cross-sections.

$$\Delta P = P_{c-neck} - P_{c-front} > 0 \quad (3)$$

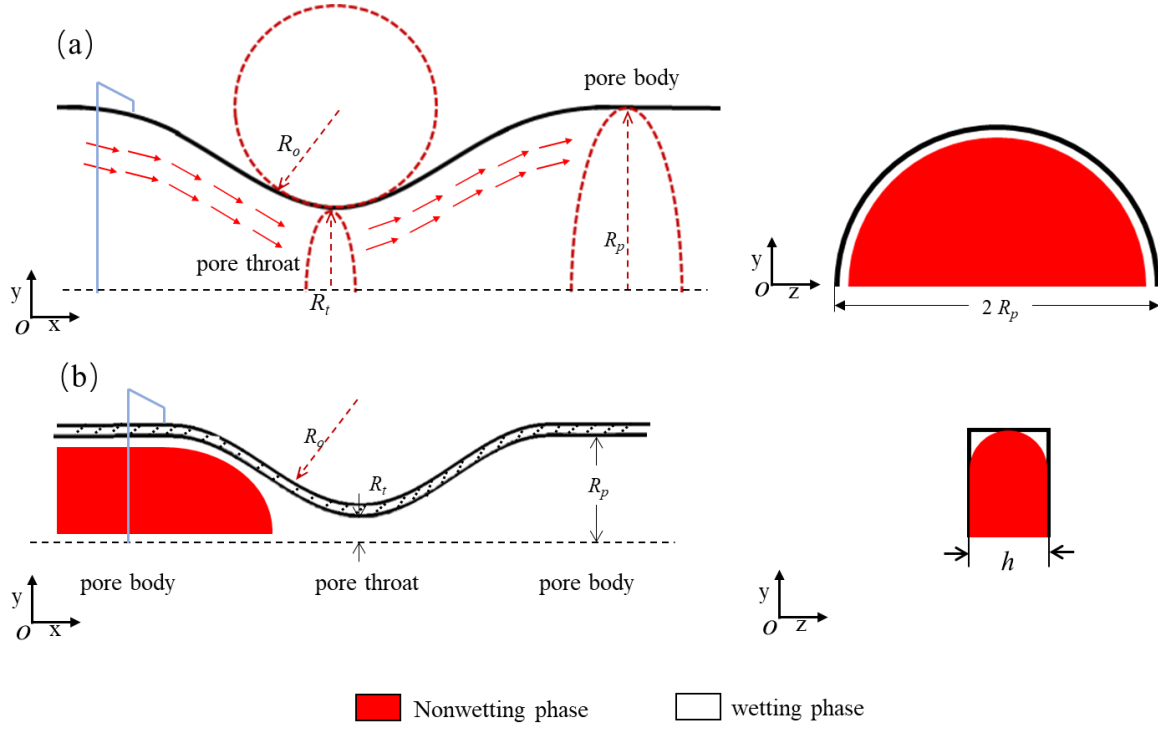


Fig. 1. Schematic of (a) the cylinder pore-throat geometry with a circular cross-section and (b) the 2D pore-throat geometry with a rectangular cross-section.

For the two dimensional (2D) pore-throat geometry which has a uniform depth (as shown in Fig. 1b), the cross-section is a rectangle, therefore, the radius of principal curvature on the y-z plane should be determined by the shorter sides of the rectangle (minimum value between the etching depth h and the pore-throat radius). Considering the relative magnitude of h against the radii R_t and R_p , there are three possibilities.

(a) $h < 2R_t$:

$$\begin{aligned} P_{c-neck} - P_{c-front} &= \sigma \left(\frac{2}{h} \cos \theta - \frac{1}{R_o} \right) - \sigma \left(\frac{2}{h} + \frac{1}{R_p} \right) \cos \theta \\ &= -\sigma \left(\frac{1}{R_o} + \frac{1}{R_p} \cos \theta \right) \end{aligned} \quad (4)$$

Since the principal curvatures on the y-z plane are all $2\cos \theta / h$, the difference in capillary pressure is only determined by the curvature difference on the x-y plane, which is always negative during the invading process. Therefore, capillary snap-off will never occur when $h < 2R_t$.

(b) $2R_t \leq h \leq 2R_p$:

$$\begin{aligned} P_{c-neck} - P_{c-front} &= \sigma \left(\frac{1}{R_t} \cos \theta - \frac{1}{R_o} \right) - \sigma \left(\frac{1}{R_p} + \frac{2}{h} \right) \cos \theta \\ &= \sigma \left(\frac{1}{R_t} \cos \theta - \frac{1}{R_o} - \frac{1}{R_p} \cos \theta - \frac{2}{h} \cos \theta \right) \end{aligned} \quad (5)$$

In this case, the principal curvatures on the y-z plane at the throat and the pore body are $1/R_t$ and $2\cos \theta / h$ respectively. As a result, the etching depth h determines the capillary pressure difference. According to Eq. (3), the snap-off criterion in terms of h is derived as

$$h_c \leq h \leq 2R_p, \quad (6)$$

145 where

$$146 \quad h_c = \frac{2}{\frac{1}{R_t} - \frac{\cos \theta}{R_o} - \frac{1}{R_p}} = \frac{2R_t R_o R_p}{R_o R_p - \cos \theta R_t R_p - R_t R_o} \quad (7)$$

147 This suggests there exists a critical depth h_c to ensure the possibility of snap-off in the pore-throat channel with a
148 rectangular cross-section.

149 (c) $h > 2R_p$:

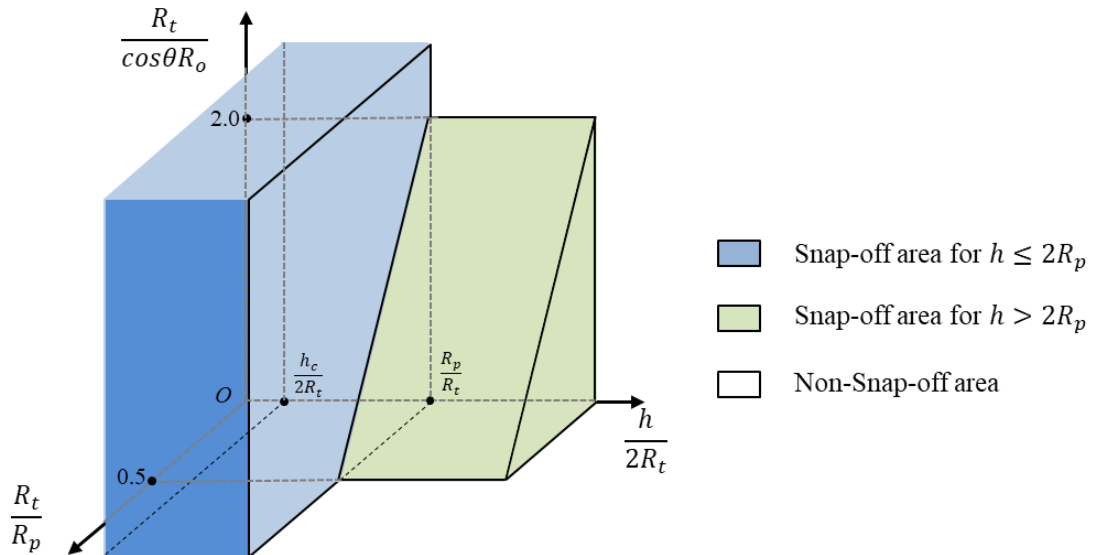
$$150 \quad \begin{aligned} P_{c-neck} - P_{c-front} &= \sigma \left(\frac{\cos \theta}{R_t} - \frac{1}{R_o} \right) - \sigma \cdot \frac{2 \cos \theta}{R_p} \\ &= \sigma \left(\frac{\cos \theta}{R_t} - \frac{1}{R_o} - \frac{2 \cos \theta}{R_p} \right) \end{aligned} \quad (8)$$

151 In this case, the principal curvatures on the y-z plane are independent of h . However, snap-off will still occur if
152 the pore-throat geometric parameters follow the criterion below, which is the same as the criterion for the
153 pore-throat with circular cross-section.

$$154 \quad R_t < \frac{R_p R_o}{R_p + 2 \cos \theta R_o} \quad (9)$$

155 Therefore, based on the above snap-off criteria for the nonwetting fluid in pore-throat channels with a
156 rectangular cross-section, we introduce a diagram to determine the possibilities of snap-off according to the
157 geometric parameters, as shown in Fig.2.

158



159

160 Fig. 2. The diagram to determine the snap-off of the nonwetting fluid in the pore-throat channel with a rectangular
161 cross-section.

162

163

164 3. Numerical modeling

165 In this section, we numerically verify the above theoretical derivations using the volume of fluid (VOF)
166 method (Brackbill et al., 1992).

3.1 Governing equations

For each phase of the fluids including the wetting fluid and the nonwetting fluid (both are assumed incompressible), the following governing equations are applied to ensure mass and momentum conservation.

$$\nabla \cdot (\rho \mathbf{U}) = 0 \quad (10)$$

$$\frac{\partial(\rho \mathbf{U})}{\partial t} + \nabla \cdot (\rho \mathbf{U} \mathbf{U}) + \nabla P = \mu \nabla \cdot (\nabla \mathbf{U} + \nabla \mathbf{U}^T) + \mathbf{F} \quad (11)$$

where \mathbf{U} is the velocity, P is the pressure, ρ is the volume-averaged density, μ is the volume average dynamic viscosity, and \mathbf{F} is the body force containing the surface tension force \mathbf{F}_s .

The continuous surface force (CFS) model by Brackbill et al. (1992) is applied to calculate \mathbf{F}_s as

$$\mathbf{F}_s = \sigma \kappa \mathbf{n} \quad (12)$$

where \mathbf{n} is the unit vector normal to the interface between two phases, and κ is the radius of curvature at the interface ($\kappa = -\nabla \cdot \mathbf{n}$) (Rossen, 2003). To consider the wettability on the non-slip wall boundary, the unit vector normal to the interface at the contact line ($\mathbf{n}|_w$) is given by (Issa, 1986)

$$\mathbf{n}|_w = \mathbf{n}_w \cos \theta + \mathbf{s}_w \sin \theta \quad (13)$$

where \mathbf{n}_w and \mathbf{s}_w are the unit vectors in the normal and tangential direction on the wall, respectively.

In the VOF method, each fluid is marked and tracked by the volume fraction that is solved by the following equation:

$$\frac{\partial \alpha_i}{\partial t} + \mathbf{U} \cdot \nabla \alpha_i = 0 \quad (14)$$

where the indicator function α denotes the volume fraction of fluid contained in each cell and the subscript i represents either wetting (w) or nonwetting (nw) phase. In each individual cell, the volume fractions of all phases are strictly conserved as $\sum \alpha_i = 1$. The interface between two phases is described by marking the volume of the cell between 0 and 1 as

$$\alpha_i = \begin{cases} 0 & \text{if cell } i \text{ is filled with oil} \\ 0 < \alpha_i < 1 & \text{the interface is in cell } i \\ 1 & \text{if cell } i \text{ is filled with water} \end{cases} \quad (15)$$

Then the average volume properties are calculated by weighting the volume fraction of oil (α_o) and water (α_w), as

$$\rho_{ave} = \alpha_o \rho_o + \alpha_w \rho_w \quad (16)$$

$$\mu_{ave} = \alpha_o \mu_o + \alpha_w \mu_w \quad (17)$$

The above momentum equation is solved by using the improved pressure implicit splitting operator (PISO) algorithm (Renardy & Renardy, 2002). The geometric reconstruction scheme (Kashchiev, 2003) is applied to solve the volume fraction equation. The second-order implicit method is applied for the discretization of temporal derivatives.

3.2 The 2D pore-throat geometry and fluid properties

We utilize 2D pore-throat geometries with various depths in our simulations. The schematic of the geometry and initial fluid distributions on the x-y plane are illustrated in Fig. 3. The geometric parameters and fluid

properties are listed in Table 1. Similar to (Rossen, 2003; Starnoni & Pokrajac, 2018; Tiznado et al., 2018), the wall profile of this geometry is described by the radius of the pore channel λ , which is designed as a function of distance in the x -direction as

$$\lambda(x) = R_p (1 - 0.5 \cdot \cos(2\pi x / L_c)) \quad (18)$$

where R_p is the radius of the pore channel, and L_c is the length of the pore constriction, which are listed in Table 1. Therefore, using this function, the expression for the radius of curvature at the throat (R_o) in Table 1 is derived as

$$R_o(x) = \sqrt{(R^2 \cdot \pi^2 \sin(2\pi x)^2 + 1)^2} / (2R \cdot \pi^2 \cos(2\pi x)) \quad (19)$$

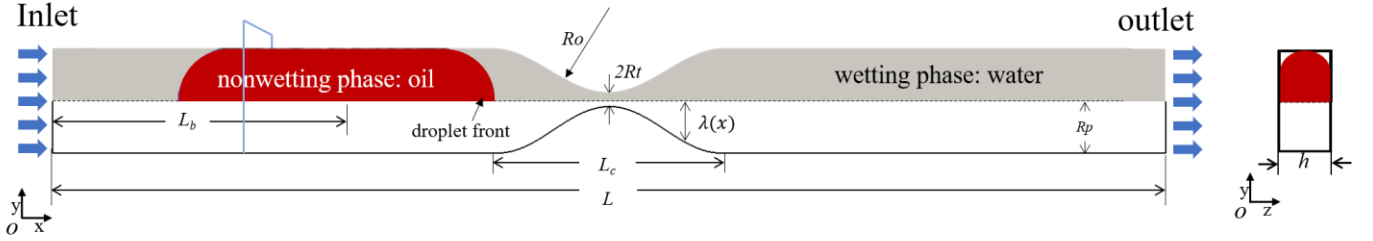


Fig. 3 Schematic of the 2D pore-throat geometry and initial fluid distributions in the simulations (red represents the non-wetting phase, and blue represents the wetting phase).

Initially, the size of the oil droplet is set as 0.6mm long and 0.24mm in diameter. We use a constant flow rate boundary at the inlet, and a constant pressure boundary is applied at the outlet. The channel wall is made to be water-wet with a contact angle of 30 degrees. The simulation parameters including geometric parameters and fluid properties are listed in Table 1 and Table 2, respectively, resulting in a capillary number (Ca) of 2×10^{-5} , which ensures that the flow is mainly governed by the capillary force (Rossen, 2003; Starnoni & Pokrajac, 2018; Tiznado et al., 2018). We use 500 μ m for the initial distance from the drop center to the inlet boundary L_b , which makes any boundary effects negligible. The grid resolution for these simulations is at least $80 \times 40 \times 15$ to ensure accuracy. More details on the convergence tests and the effect of the inlet boundary are presented in the Appendix A.

Table 1. Geometric parameters used for simulations

model type	Constriction length, L_c (μ m)	drop center to inlet, L_b (μ m)	Radius of throat, R_t (μ m)	principal curvature, R_o (μ m)	Radius of pore body, R_p (μ m)	Total length, L (μ m)	Critical depth, h_c (μ m)
Geometry 1	500	500	14	120	121.78	2500	37.3
Geometry 2	400	500	24	60	60	200	2500

Table 2. fluid properties used for simulation

Contact angle, θ	Surface tension, σ	Flow rate, Q	Capillary number, Ca	Density of oil, ρ_o	Density of water, ρ_w	Oil viscosity, μ_o	Water viscosity, μ_w	Bubble length, L_b
degree	N/m	μ L/h	dimensionless	g/cm ³	g/cm ³	Pa·s	Pa·s	μ m
30	0.072	50	2×10^{-5}	0.937	1	0.015	0.001	600

3.3 Numerical results for different categories

In the following simulations, the etching depth h is varied to correspond to the three categories we have proposed in Section 2.

228 (a) $h < 2R_t$:

229 Our theoretical analysis has indicated that capillary snap-off will never occur when the etching depth is less
 230 than twice the throat radius. This is verified by performing the following two simulations using different depths as
 231 $h=10\text{ }\mu\text{m}$ and $h=25\text{ }\mu\text{m}$ on geometry 1, which are both less than $2R_t$ ($28\text{ }\mu\text{m}$).

232 The displacing processes for these two cases are shown in Fig. 3. In both cases, the droplets pass through the
 233 throat smoothly and the snap-off never occurs. During the process, the pressure at the throat is always less than the
 234 pressure at the droplet front. Therefore, these results confirm our theoretical analysis for this category.

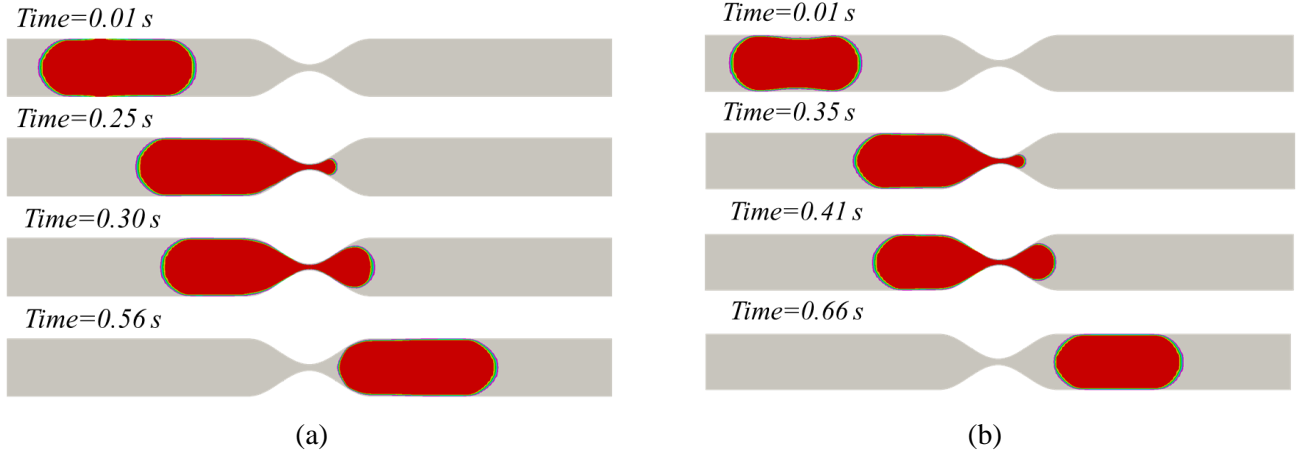


Fig. 4 Time evaluation of volume fraction in the pore-throat geometries of (a) $h=10\text{ }\mu\text{m}$ and (b) $h=25\text{ }\mu\text{m}$.

239 (b) $2R_t \leq h \leq 2R_p$:

240 Our theoretical analysis has indicated there exists a critical depth h_c for the occurrence of snap-off. According
 241 to Eq. (6) and the geometric parameters, this depth is calculated as $h_c=37.3\text{ }\mu\text{m}$. Therefore, to verify this, we
 242 perform another two simulations using different depths as $h=35\text{ }\mu\text{m}$ and $h=40\text{ }\mu\text{m}$ on geometry 1.

243 The simulation results for these two cases are shown in Fig. 4. In the pore-throat channel of $h=40\text{ }\mu\text{m}$ (Fig.
 244 4(b)), which is greater than the critical depth, the snap-off occurs; while for the case of $h=35\text{ }\mu\text{m}$ (Fig. 5(a)),
 245 snap-off never occurs since h is smaller than the critical depth. For the case where snap-off occurs ($h=40\text{ }\mu\text{m}$), the
 246 pressure at the throat is greater than the pressure at the droplet front at the snap-off moment. For the case where
 247 snap-off never occurs ($h=35\text{ }\mu\text{m}$), the pressure difference at the throat and the droplet front remains negative. These
 248 results are all in good agreement with our theoretical analysis for this category.

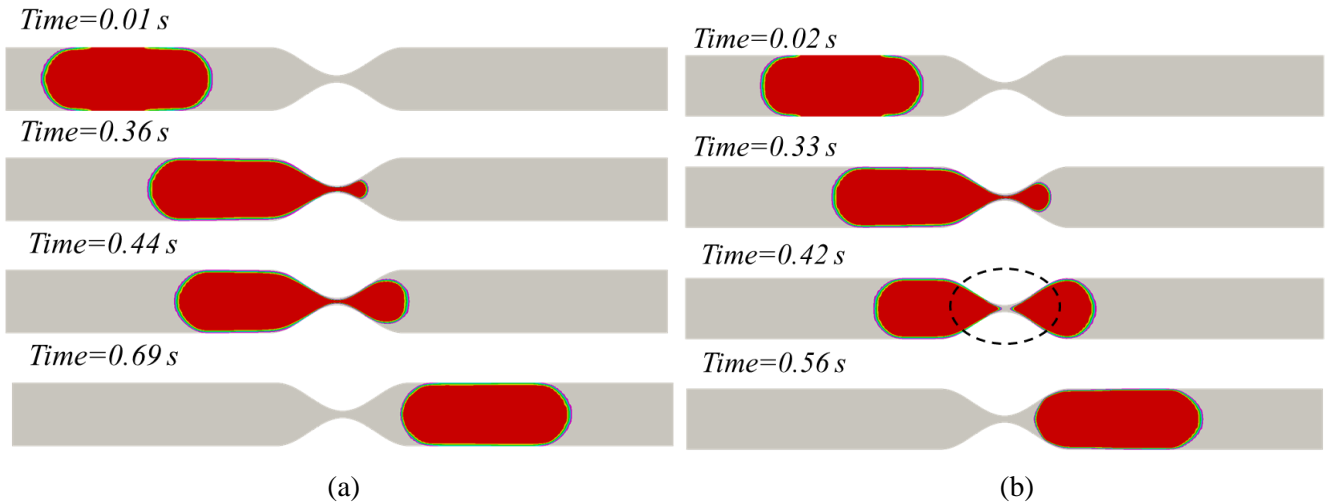


Fig. 5 Time evaluation of volume fraction in the pore-throat geometries of (a) $h=35\text{ }\mu\text{m}$ and (b) $h=40\text{ }\mu\text{m}$.

(c) $h > 2R_p$:

Our theoretical analysis shows that the snap-off criterion is independent with h when $h > 2R_p$. Since the geometric parameters satisfy Eq. (8), snap-off will occur in the geometry we considered. Again, to verify the theoretical derivation, simulations are performed using different depths as $h=250\text{ }\mu\text{m}$ and $h=300\text{ }\mu\text{m}$ on geometry 1, which are both greater than $2R_p$ ($240\mu\text{m}$).

The displacing processes for these two cases are shown in Fig.5. In both cases, the snap-off occurs at the throat of the channel. At the snap-off moment, the pressure at the throat is greater than the pressure at the droplet front.

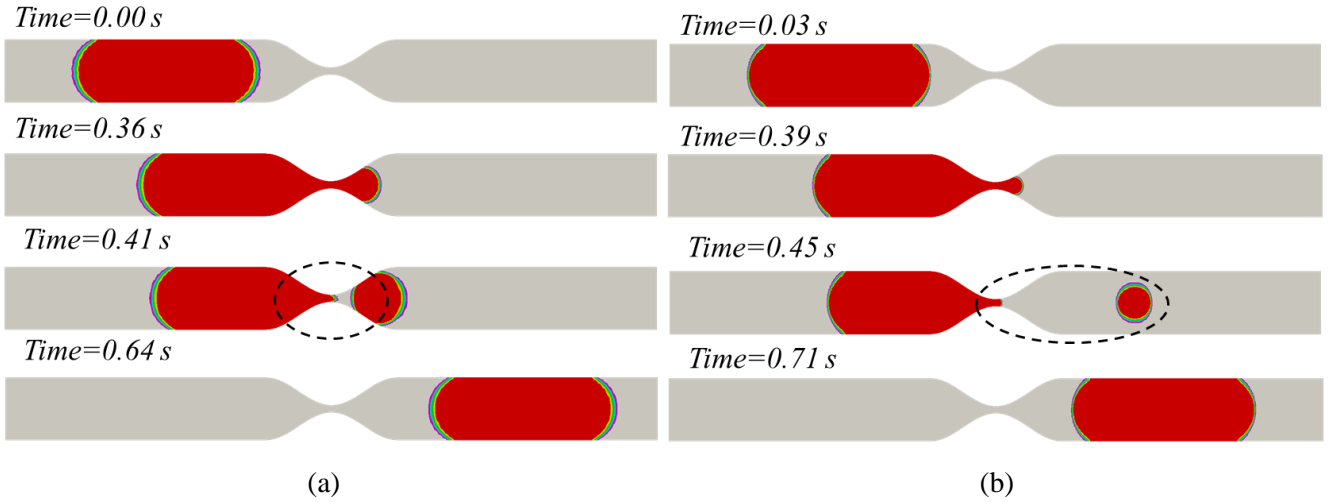


Fig. 6 Time evaluation of volume fraction in the pore-throat geometries of (a) $h=250\text{ }\mu\text{m}$ and (b) $h=300\text{ }\mu\text{m}$.

If Eq. (9) is not satisfied, snap off will never occur. To verify this criterion, we design another geometry (geometry 2) with a new group of geometric parameters which leads to $R_t > \frac{R_p R_o}{R_p = 2 \cos \theta R_o}$. The simulation result for this case is shown in Fig. 7, which shows that snap-off does not occur.

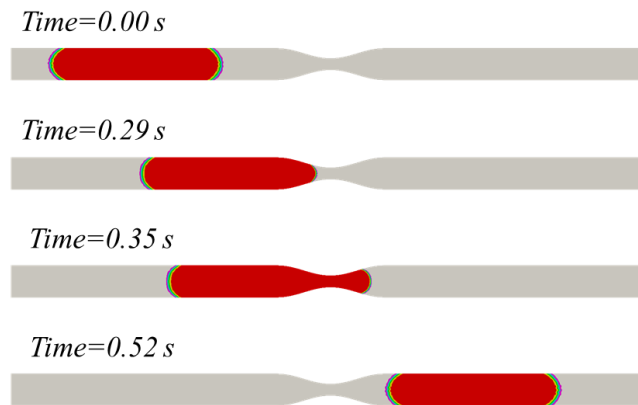


Fig. 7 Time evaluation of volume fraction in the pore-throat geometry 2.

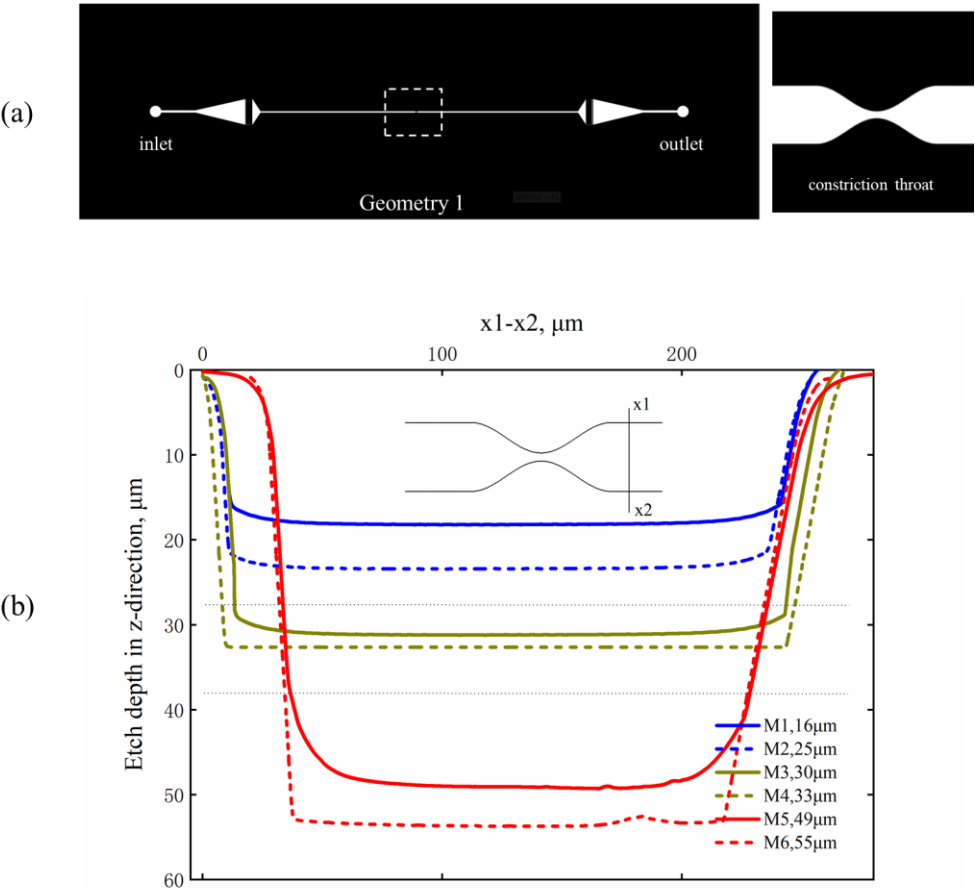
4. Microfluidic experiments

The above simulation results verify the theoretical analysis of the snap-off criteria under different circumstances. In this section, we further examine the validity of these criteria in microfluidic channels.

4.1 Microchannel fabrication

276
277
278
279
280
281
282
283
284
285
286
287
288
289
290
291

The pore-throat channels with the geometric parameters described in Table 1 were utilized in the lithography mask (2.5 inches by 0.75 inch in size), as shown in Fig. 8(a). The pore channel was etched on silicon wafers in a Class 10 cleanroom environment and all the wafers were 2 inches in diameter and 500 μm thick, single side polished and the crystal direction is N <1,0,0>. The silicon wafers were chemically cleaned by the developed standard clean procedure (Kern, 1990) to remove the contaminant films and discrete particles. The primed wafers were dehydrated at 150°C for 30 minutes using HMDS (Hexamethyl Disilazane) allowing better coverage and adhesion with photoresist. Then, the wafers were spin-coated with a thin layer of positive photoresist on the surface. Next, the silicon wafers were selectively exposed to ultraviolet light using the SUSS MA6 contact aligner with a dosage of 150 mJ/cm^2 . The exposed area was washed from the silicon surface by using a developer solution, and the remaining photoresist served as etch protector. Then, the wafers were rinsed with DI water and dried with nitrogen before hard-bake at 110°C for 10 minutes. After lithography, the exposed area of silicon wafers was etched to different depth respectively, which was determined by our simulation geometry structures. The dry etching process was performed by Oxford Instruments Plasma Lab 80+. The deep reactive ion etching (DRIE) method was conducted and fluorine plasma was used as the etching gas. More etching details can be found in Ref. (Li et al., 2001; Kolari et al., 2008 Buchgraber et al., 2012).



292
293
294
295
296

Fig. 8 Geometry of the silicon wafers (a) photomask for the microchannel with a constriction throat; and (b) etching depth profiles of each silicon wafer at the line x1-x2 (M1:16 μm , M2:25 μm , M3:30 μm , M4:33 μm , M5:49 μm , and M6:55 μm).

297
298
299
300
301

After etching, the wafer was cleaned using sulfuric acid and hydrogen peroxide at a ratio of 1:9. Then, the inlet and outlet were drilled at both ends of the microchannel using an ultrasonic disk cutter. Next, the wafers were cleaned by distilled water and the etched wafer was sealed with a plain glass cover (1mm thickness, BOROFLOAT®33, Schott) hermetically by the anodic bonding process (Alcalde et al., 2019) to create a 2D flow path with a rectangular cross-section.

The fabrication procedure was used to create three groups of microfluidic chips that fall into the two categories ((a) and (b) in Section 3) by varying the etching depth, as shown in Table 3. The etching depth profiles of each silicon wafer are measured by the Dektak 6M Stylus Profilometer, as presented in Fig.8(b). Group 1 (G1) falls into category (a), where the etching depth h_{et} is smaller than the throat size ($h_{et} < 2R_t$). The other two groups fall into category (b): for Group 2 (G2), the etching depth is in between the pore throat size and critical depth ($2R_t < h_{et} < h_c$); for Group 3, the etching depth is deeper than the critical depth ($h_{et} > h_c$). Because of the limitation in the etching depth, we are not able to create a microchannel that falls into category (c), where h_{et} should be larger than the pore size ($h > 2R_p$).

Table 3. Silicon-etched microfluidic chips used in the experiments

Groups	Model Number	Etching Time	Etching Depth	Depth range
G 1	M1	8 mins	16 μm	$h_{et} < 2R_t$
	M2	10 mins	25 μm	
G 2	M3	22 mins	30 μm	$2R_t < h_{et} < h_c$
	M4	25 mins	33 μm	
G 3	M5	30mins	49 μm	$h_{et} > h_c$
	M6	35mins	55 μm	

4.2 Experimental procedure

The experimental system is shown in Fig.9. The etched-silicon microchannel was horizontally mounted in an aluminum holder and the syringe (Hamilton, 1000 series, 5ml) was connected to the inlet of the microchannel. The injection rates were controlled by a syringe pump (Harvard Apparatus 2000). The outlet was open to the atmosphere downstream. The fluid behavior within the microchannel was visualized by a confocal microscope, and images were captured using the mounted camcorder (Zeiss Axioscope).

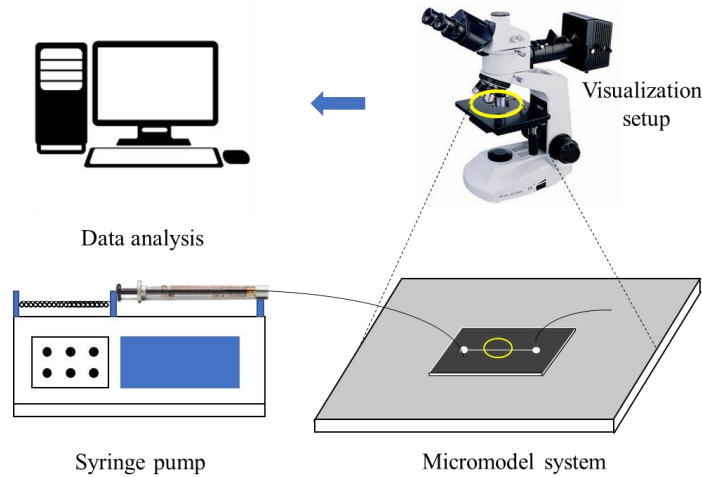


Fig. 9 The microfluidic experimental system for visualizing flow behavior.

For all experiments, the nonwetting phase is a mixture of mineral oil and decane (85% of mineral oil and 15% of decane, 35cp at 25°C) and deionized water (DI water) is the wetting phase. The fluid properties are listed in Table 1. Before each flooding experiment, the microchannel was thoroughly cleaned using isopropanol, DI water, and compressed air. Then the microchannel was saturated with DI water and aged for 24 hours until no trapped gas was left in the channel. Finally, the oil mixture was injected into the channel at a constant rate of $Q = 5 \mu\text{l}/h$.

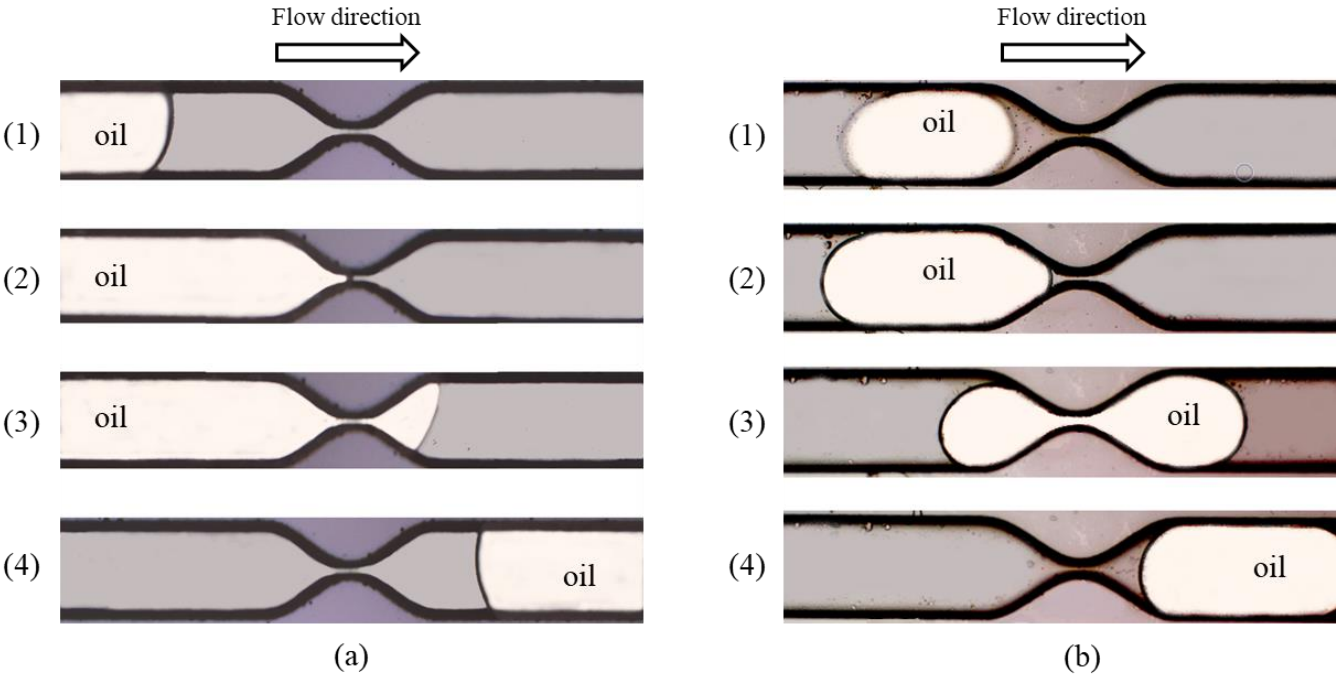
Correspondingly, the capillary number $Ca = \frac{\mu v}{\sigma} \approx 1.2 \times 10^{-4}$, which is close to our simulation conditions.

328

329 4.3 Displacing results

330 (a) $h < 2R_t$:

331 The experimental results for microchannels M1 and M2 are shown in Fig. 10, of which the depths are smaller
332 than the critical depth. As expected, snap-off does not occur and the oil went through the constriction throat as a
333 continuous phase.



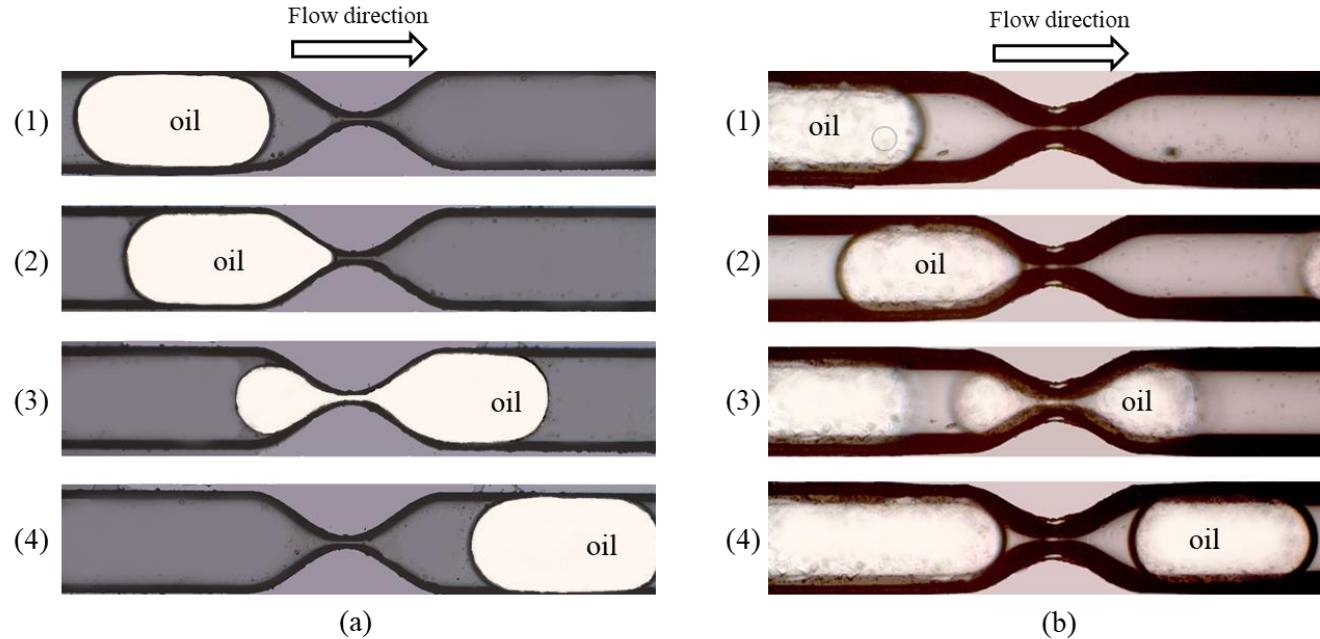
334

335 Fig. 10 Displacing results for (a) M1: etching depth=16 microns, and (b) M2: etching depth=25 microns.

336

337 (b) $2R_t \leq h \leq 2R_p$:

338 Fig. 11 shows the results for microchannels M3 and M4, of which the depths are in between the pore-throat
339 and the critical depth. Capillary snap-off does not occur as predicted by the theory.



340

Fig. 11 Displacing results for (a) M3: etching depth=30 microns, and (b) M3: etching depth=33 microns.

However, for microchannels M5 and M6, whose etching depths are larger than the critical depth, the oil droplet is trapped at the pore throat and snap-off occurs at the constriction, as shown in Fig. 12.

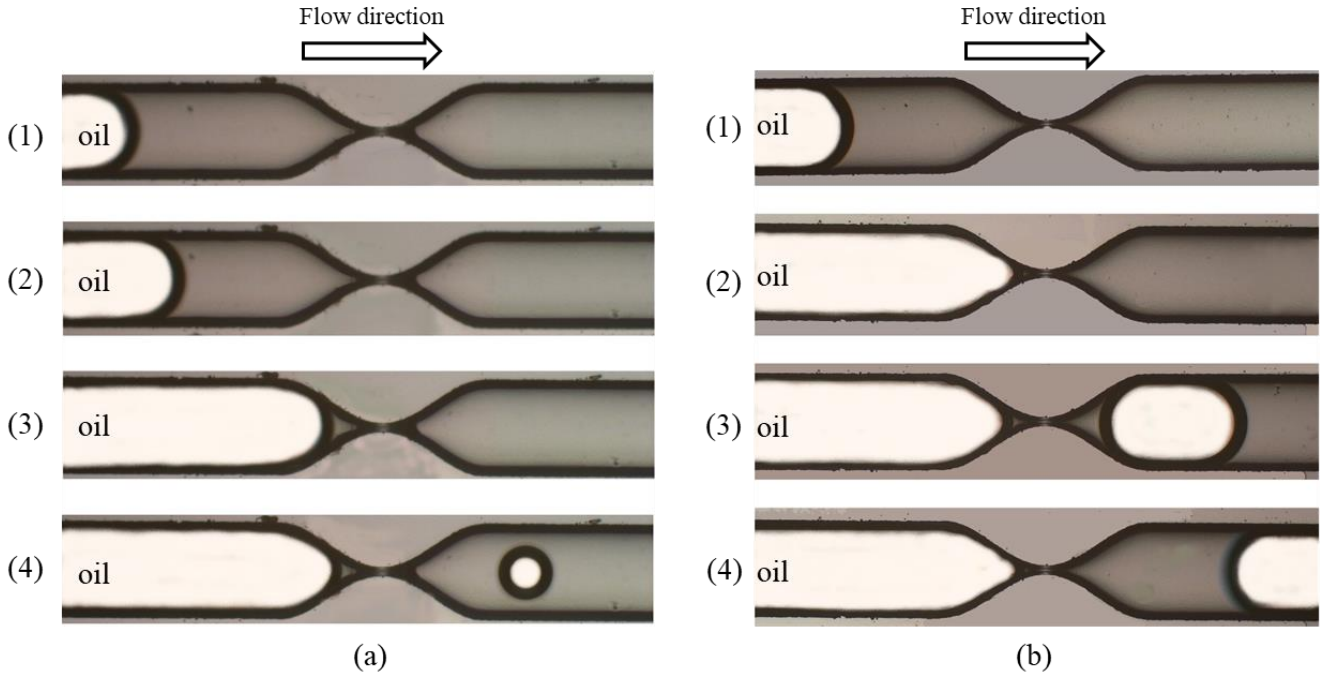


Fig.12 Displacing results for (a) M3: etching depth=49 microns, and (b) M3: etching depth=55 microns. Note: the color difference is resulted to the reflection light difference

The simulation and experimental results are plotted onto the 2D diagrams converted from the 3D diagram (Fig. 2), as shown in Fig.13. All the data fall into the area predicted by the theoretical criteria, which supports our theoretical analysis. We also included additional simulation results based on other geometries with different ratios of R_t/R_o (listed in Appendix B) and marked them on the diagrams.

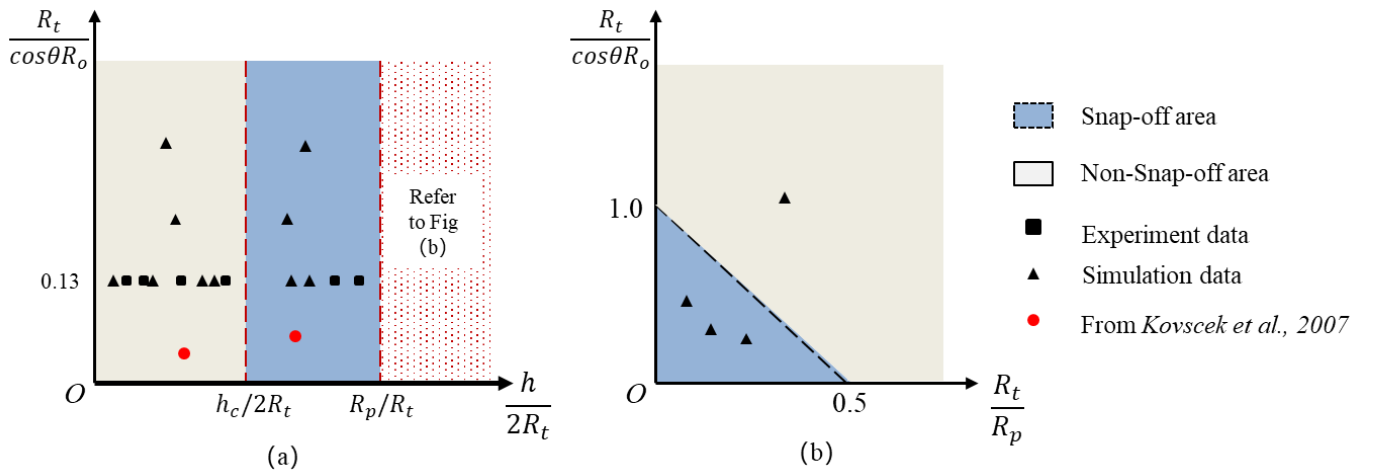
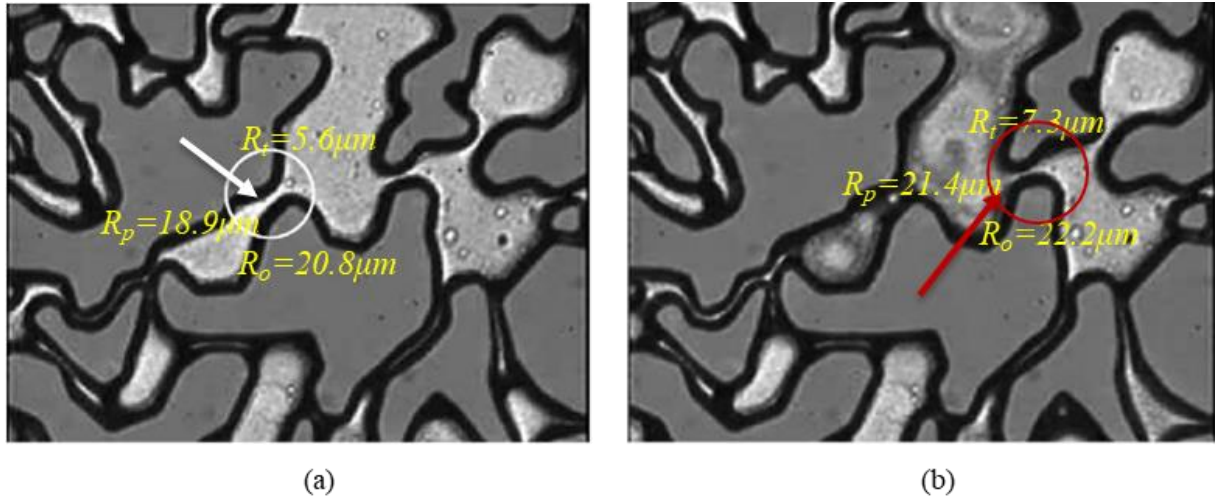


Fig. 13 2D diagrams for the snap-off criteria in the pore-throat channel with a rectangular cross-section: (a) $h < 2R_p$, and (b) $h > 2R_p$.

By applying these criteria, we further investigate the snap-off behavior that was observed in Kovscek et al.'s 2D micromodel (Kovscek et al., 2007), as shown in Fig. 14. Our calculation shows that the local pore-throat geometry (Fig. 14(a)) with the estimated geometrical parameters ($R_t=5.6 \mu\text{m}$, $R_p=18.9 \mu\text{m}$, $R_o=20.8 \mu\text{m}$ and $h=25$

360 μm) satisfies our criteria for snap-off as $2R_p > h = 25\mu\text{m} > h_c = \frac{2R_t R_o R_p}{R_p R_o - \cos\theta R_t R_p - R_t R_o} = 21.23\mu\text{m}$; while the
 361 geometry shown in Fig.14(b) with parameters ($R_t=7.3\mu\text{m}$, $R_p=21.4\mu\text{m}$, $R_o=22.2\mu\text{m}$ and $h=25\mu\text{m}$) suppressed the
 362 snap-off because $2R_t < h = 25\mu\text{m} < h_c = \frac{2R_t R_o R_p}{R_p R_o - \cos\theta R_t R_p - R_t R_o} = 33.5\mu\text{m}$. These estimated data are included the
 363 above 2D diagrams (Fig. 13) as well.



364
 365 Fig.14 Observations in Kovscek et al. (2007): (a) snap-off occurred at the white circled area; (b) snap-off was
 366 suppressed at the red circled area.
 367

368 5. Implications and Discussion

369 A common occurrence of rectangular cross-sections of microchannels is the pore throats in 2D micromodels
 370 used to study multiphase flow in porous media, which have a uniform depth due to the selectivity and anisotropy of
 371 the etching methods. Snap-off is an important phenomenon that occurs frequently in naturally-occurring porous
 372 media; therefore, micromodels should be able to allow snap-off if they are to be used as tools for studying
 373 multiphase flow in porous media. There has been some debate as to whether snap off is possible in 2D
 374 micromodels. Rossen (2008) and Xu et al. (2017) claimed that snap off was difficult or impossible in 2D
 375 micromodels, but Kovscek et al. (2007) showed snap-off did occur in their experiments (their data agree with
 376 criteria in Fig 13). Our analysis shows that snap off is possible in 2D media, but the depth, h , must be relatively
 377 large and meet the derived criteria. It is laborious and costly to ensure the precise vertical structures, good
 378 uniformity of the wafer and the high depth-to-width ratio simultaneously for a deep etching. Therefore, the
 379 inclusion of three-dimensional features, such as the 2.5D micromodel (Xu et al., 2017) may be most suitable for
 380 studying snap off in micromodels.

381 6. Conclusions

382 In this study, capillary snap-off in 2D pore-throat microchannels with a rectangular cross-section are
 383 systematically studied. Geometric criteria for the occurrence of snap-off are theoretically derived. Based on the
 384 range of etching depth h , the criteria are divided into three categories: (a) if h is smaller than the width of the throat,
 385 snap-off will never occur; (b) if h is larger than the width of the pore, snap-off may occur but the criterion is
 386 independent of h ; (c) if h is larger than the throat width and smaller than the pore width, snap-off will occur when a
 387 critical depth is reached. Then numerical simulations using OpenFOAM are performed to verify these criteria. In
 388 the simulations, pore-throat geometries with various depths are designed according to the three categories. In all the
 389 cases, the simulation results agree well with our theoretical predictions, which illustrates the correctness of the
 390 criteria. We also perform microfluidic experiments to further examine the validity of these criteria. The
 391 experimental results are also in agreement with the theoretical analysis. These results clarify the previous debates

on whether the 2D micromodels for flow in porous media are suitable for snap-off studies. If the 2D micromodel follows the geometric criteria we proposed, snap-off will occur. Therefore, this work provides new guidelines for the design of micromodels with a rectangular cross-section to account for the snap-off phenomenon. However, inclusion of 3D features in micromodels are recommended because large etching depths in 2D micromodels can be challenging and 3D features additionally allow for continuity of the grain phase.

Acknowledgments

We would like to thank Mr. Lucas Mejia, Ms. Yujing Du and Dr. Shunxiang Xia for helping with the microchannel fabrication. Mr. Cha and Dr. Feng acknowledge the National Nature Science Foundation of China (Grant No. 51474233), State Major Science and Technology Special Projects during the 13th Five-Year Plan (Grant No. 2016ZX05011-001), the Program for Chengjiang Scholars and Innovation Research Team in University (IRT1294), National Postdoctoral Program for Innovative Talents (BX201600153), and Fundamental Research Funds for the Central Universities (Grant No. 18CX07006A). Dr. Xie and Dr. Balhoff acknowledge the Chemical EOR Industrial Affiliates Project in the Center for Subsurface Energy and the Environment at The University of Texas at Austin for the financial support and the Texas Advanced Computing Center (TACC) at The University of Texas at Austin for providing the computing resources. We note that there are no data sharing issues since all of the numerical information is provided in the tables and figures produced by solving the equations in the paper.

Appendix A: Convergence tests and the inlet boundary effect

Here we are to present the convergence tests and a discussion on the effect of the inlet boundary by varying the mesh size and the length L_b .

For the convergence tests, we construct four different meshes (Fig. A1) for the same geometry with parameters satisfying Eq. (9) as listed in Table A1. The initial distance from the drop center to the inlet L_b is set as $500\mu\text{m}$. The displacements calculated by different meshes are shown in Fig. A2. As is seen, the coarsest mesh ($60\times 20\times 10$) is not enough to correctly capture the snap-off, while the other three meshes are sufficient. Also note that the results obtained by $80\times 40\times 15$ grids are close to the finest-mesh ($100\times 50\times 20$) results, therefore, we employ the mesh size of $80\times 40\times 15$ for the simulations in the main text considering the balance between numerical accuracy and efficiency.

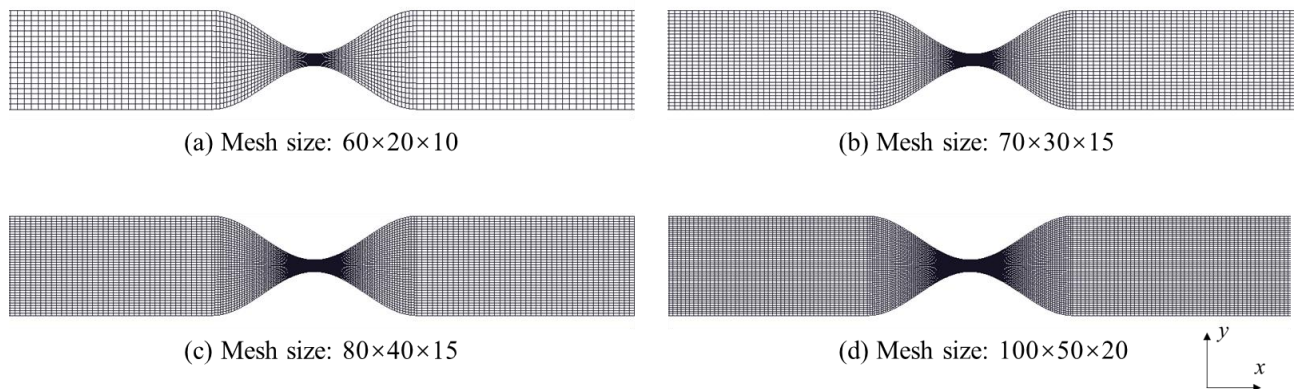


Fig. A1 Four different meshes for the convergence study. (a) $60\times 20\times 10$, (b) $70\times 30\times 15$, (c) $80\times 40\times 15$, and (d) $100\times 50\times 20$.

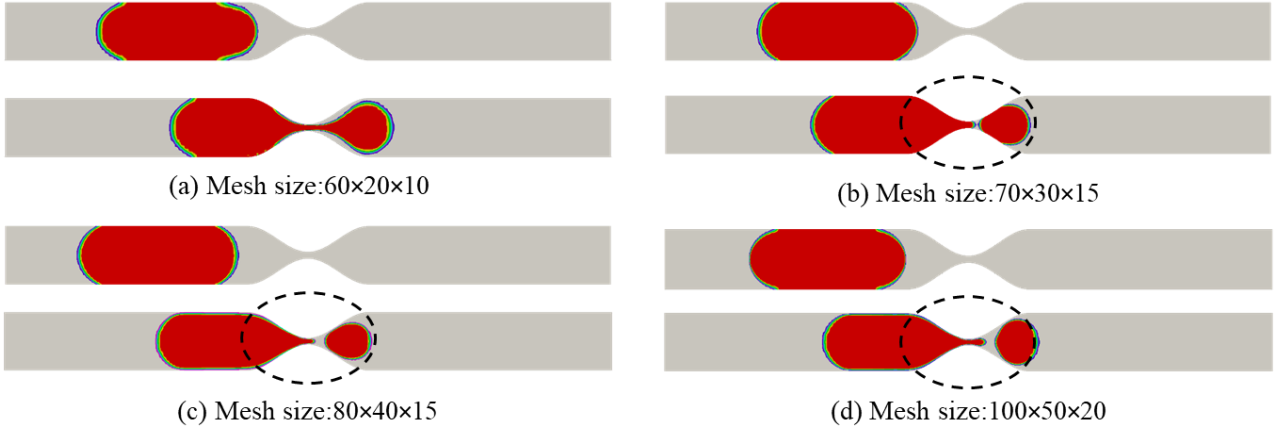


Fig. A2 The displacements obtained by different meshes of (a) $60 \times 20 \times 10$, (b) $70 \times 30 \times 15$, (c) $80 \times 40 \times 15$, and (d) $100 \times 50 \times 20$.

Table A1. Geometric parameters for the convergence tests and the inlet boundary effect.

Parameters	Values	units
Radius of throat, R_t	14	μm
Radius of principal curvature, R_o	120	μm
Radius of pore body, R_p	121.78	μm
Total length, L	2500	μm
Depth, h	40	μm
Physical time step	0.0001	s
Number of grids	$60 \times 20 \times 10$	
	$70 \times 30 \times 15$	
	$80 \times 40 \times 15$	
	$100 \times 50 \times 20$	
Initial distance from drop center to inlet, L_b	300, 500, 700	μm

For the effect of the inlet boundary, we discuss three different initial positions of the nonwetting fluid by varying the lengths L_b from $300\mu\text{m}$ to $700\mu\text{m}$. Fig. A3 (a) compares the streamlines downstream of the droplets when they approach the throat and Fig. A3 (b) plots the average velocity of the droplet at that moment against L_b . For $L_b = 300\mu\text{m}$, the streamlines are unstable, while for L_b larger than $500\mu\text{m}$, the streamlines are stable and of the same pattern. The variation in the average velocity also decreases when L_b is larger than $500\mu\text{m}$. These results illustrate that the inlet boundary effect can be ignored when $L_b \geq 500\mu\text{m}$. As a result, the initial distance from the drop center to the inlet is set at $500\mu\text{m}$ for all the simulations in the main text.

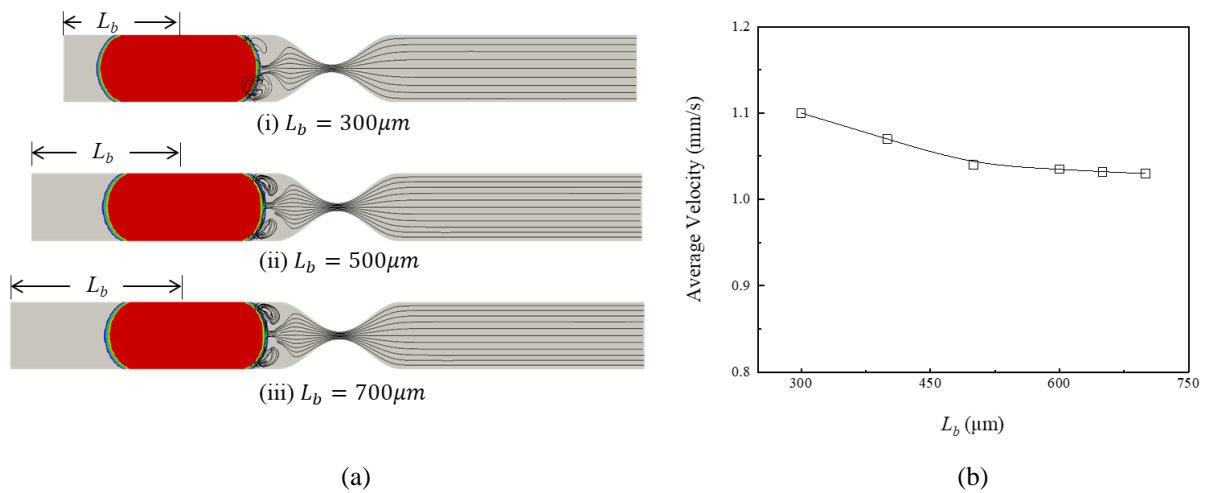


Fig. A3 The effect of inlet boundary on (a) the streamlines and (b) the average velocity of the droplet when getting close to the throat.

Appendix B: simulation results for different geometry structures

In this section, we add additional simulations using geometries with different ratios of R_t/R_o to enrich the data marked in Fig. 13. Details of these geometries are listed in Table B1.

Table B1. Geometric parameters used for simulations

Model No.	Radius of throat, R_t (μm)	principal curvature, R_o (μm)	Radius of pore body, R_p (μm)	Critical depth, h_c (μm)	Simulation Depth, h (μm)	Simulation results
S1	16	111.3	110	43.9	30	Non-snap-off
S2	16	111.3	110	43.9	50	snap-off
S3	16	111.3	110	43.9	300	snap-off
S4	28.33	176.7	100	98.1	50	Non-snap-off
S5	28.33	176.7	100	98.1	120	snap-off
S6	28.33	176.7	100	98.1	400	snap-off

References

- Afsharpoor, A., & Javadpour, F. (2016). Liquid slip flow in a network of shale noncircular nanopores. *Fuel*, 180, 580–590. <https://doi.org/10.1016/j.fuel.2016.04.078>
- Alcalde, R. E., Michelson, K., Zhou, L., Schmitz, E. v., Deng, J., Sanford, R. A., et al. (2019). Motility of *Shewanella oneidensis* MR-1 Allows for Nitrate Reduction in the Toxic Region of a Ciprofloxacin Concentration Gradient in a Microfluidic Reactor. *Environmental Science and Technology*, 53(5), 2778–2787. <https://doi.org/10.1021/acs.est.8b04838>
- Almajid, M. M., & Kavscek, A. R. (2020). Pore Network Investigation of Trapped Gas and Foam Generation Mechanisms. *Transport in Porous Media*, 131(1), 289–313. <https://doi.org/10.1007/s11242-018-01224-4>
- Andrew, M., Bijeljic, B., & Blunt, M. J. (2014). Pore-by-pore capillary pressure measurements using X-ray microtomography at reservoir conditions: Curvature, snap-off, and remobilization of residual CO₂. *Water Resources Research*, 50(11), 8760–8774. <https://doi.org/10.1002/2014WR015970>

- Berry, S. B., Lee, J. J., Berthier, J., Berthier, E., & Theberge, A. B. (2019). Droplet incubation and splitting in open microfluidic channels. *Analytical Methods*, 11(35), 4528–4536. <https://doi.org/10.1039/c9ay00758j>
- Blunt, M. J. (1998). Physically-based network modeling of multiphase flow in intermediate-wet porous media. *Journal of Petroleum Science and Engineering*, 20(3–4), 117–125. [https://doi.org/10.1016/S0920-4105\(98\)00010-2](https://doi.org/10.1016/S0920-4105(98)00010-2)
- Brackbill, J. U., Kothe, D. B., & Zemach, C. (1992). A continuum method for modeling surface tension. *Journal of Computational Physics*, 100(2), 335–354.
- Buchgraber, M., Kovscek, A. R., & Castanier, L. M. (2012). A Study of Microscale Gas Trapping Using Etched Silicon Micromodels. *Transport in Porous Media*, 95(3), 647–668. <https://doi.org/10.1007/s11242-012-0067-0>
- Cunha, L. H. P., Siqueira, I. R., Albuquerque, E. L., & Oliveira, T. F. (2018). Flow of emulsion drops through a constricted microcapillary channel. *International Journal of Multiphase Flow*, 103, 141–150. <https://doi.org/10.1016/j.ijmultiphaseflow.2018.02.015>
- Deng, W., Cardenas, M. B., & Bennett, P. C. (2014). Extended Roof snap-off for a continuous nonwetting fluid and an example case for supercritical CO₂. *Advances in Water Resources*, 64, 34–46. <https://doi.org/10.1016/j.advwatres.2013.12.001>
- Du, Y., Mehmani, A., Xu, K., Balhoff, M., & Torres-Verdín, C. (2019). Micromodel study of the impacts of fracture connectivity and wettability on matrix sweep efficiency. *SPE/AAPG/SEG Unconventional Resources Technology Conference 2019, URTC 2019*, 1–13. <https://doi.org/10.15530/urtec-2019-144>
- Feng, Q., Cha, L., Dai, C., Zhao, G., & Wang, S. (2020). Effect of particle size and concentration on the migration behavior in porous media by coupling computational fluid dynamics and discrete element method. *Powder Technology*, 360. <https://doi.org/10.1016/j.powtec.2019.10.011>
- Herring, A. L., Gilby, F. J., Li, Z., McClure, J. E., Turner, M., Veldkamp, J. P., et al. (2018). Observations of nonwetting phase snap-off during drainage. *Advances in Water Resources*, 121(July), 32–43. <https://doi.org/10.1016/j.advwatres.2018.07.016>
- Hirt, C. W., & B.D. Nichols. (1981). volume of fluid (VOF) method for the dynamics of free boundaries. *Journal of Computational Physics*, 39(3), 201–225. <https://doi.org/10.1007/s40998-018-0069-1>
- Idowu, N. A., & Blunt, M. J. (2010). Pore-scale modelling of rate effects in waterflooding. *Transport in Porous Media*, 83(1), 151–169. <https://doi.org/10.1007/s11242-009-9468-0>
- Issa, R. I. (1986). Solution of the implicitly discretised fluid flow equations by operator-splitting. *Journal of Computational Physics*, 62(1), 40–65.
- Jasak, H., Jemcov, A., & Tukovic, Z. (2007). OpenFOAM: A C++ Library for Complex Physics Simulations. *International Workshop on Coupled Methods in Numerical Dynamics*, m, 1–20.
- Kashchiev, D. (2003). Determining the curvature dependence of surface tension. *Journal of Chemical Physics*, 118(20), 9081–9083. <https://doi.org/10.1063/1.1576218>
- Kern, W. (1990). Evolution of silicon wafer cleaning technology. *Proceedings - The Electrochemical Society*, 90(9), 3–19.
- King, U. (2013). OpenFOAM: Open source CFD in research and industry, 10–15.
- Kolari, K., Saarela, V., & Franssila, S. (2008). Deep plasma etching of glass for fluidic devices with different mask materials. *Journal of Micromechanics and Microengineering*, 18(6). <https://doi.org/10.1088/0960-1317/18/6/064010>
- Kovscek, A. R., & Radke, C. J. (1996). Gas bubble snap-off under pressure-driven flow in constricted noncircular capillaries. *Colloids and Surfaces A: Physicochemical and Engineering Aspects*, 117(1–2), 55–76. [https://doi.org/10.1016/0927-7757\(96\)03637-0](https://doi.org/10.1016/0927-7757(96)03637-0)
- Kovscek, A. R., Tang, G. Q., & Radke, C. J. (2007). Verification of Roof snap off as a foam-generation

mechanism in porous media at steady state. *Colloids and Surfaces A: Physicochemical and Engineering Aspects*, 302(1–3), 251–260. <https://doi.org/10.1016/j.colsurfa.2007.02.035>

Lamanna, J. M., Bothe, J. v., Zhang, F. Y., & Mench, M. M. (2014). Measurement of capillary pressure in fuel cell diffusion media, micro-porous layers, catalyst layers, and interfaces. *Journal of Power Sources*, 271, 180–186. <https://doi.org/10.1016/j.jpowsour.2014.07.163>

Lenormand, R., Zarcone, C., & Sarr, A. (1983). Mechanisms of the displacement of one fluid by another in a network of capillary ducts. *Journal of Fluid Mechanics*, 135, 337–353. <https://doi.org/10.1017/S0022112083003110>

Lenormand, Roland, & Zarcone, C. (1984). Role of roughness and edges during imbibition in square capillaries. *Proceedings - SPE Annual Technical Conference and Exhibition, 1984-Septe.*

Li, X., Abe, T., & Esashi, M. (2001). Deep reactive ion etching of Pyrex glass using SF₆ plasma. *Sensors and Actuators, A: Physical*, 87(3), 139–145. [https://doi.org/10.1016/S0924-4247\(00\)00482-9](https://doi.org/10.1016/S0924-4247(00)00482-9)

Lifton, V. A. (2016). Microfluidics: An enabling screening technology for enhanced oil recovery (EOR). *Lab on a Chip*, 16(10), 1777–1796. <https://doi.org/10.1039/c6lc00318d>

Mogensen, K., & Stenby, E. H. (1998). A Dynamic Two-Phase Pore-Scale Model of Imbibition. *Transport in Porous Media*, 32(1–3), 299–327. <https://doi.org/10.2118/39658-ms>

Musehane, N., & Herbst, R. (2019). Numerical Investigation of Different Dynamic Contact Angle Models for a Droplet Impacting a Surface in OpenFOAM. *Mapta Journal of Mechanical and Industrial Engineering (MJMIE)*, 3(1), 9–17. <https://doi.org/10.33544/mjmie.v3i1.96>

Picchi, D., & Battiatto, I. (2018). The Impact of Pore-Scale Flow Regimes on Upscaling of Immiscible Two-Phase Flow in Porous Media. *Water Resources Research*, 54(9), 6683–6707. <https://doi.org/10.1029/2018WR023172>

Ransohoff, T. C., & Radke, C. J. (1989). Mechanisms of foam generation in glass-bead packs. *Spe Reservoir Engineering*, 3(2, May, 1989), 573–585.

Ransohoff, T. C., Gauglitz, P. A., & Radke, C. J. (1987). Snap-off of gas bubbles in smoothly constricted noncircular capillaries. *AIChE Journal*, 33(5), 753–765. <https://doi.org/10.1002/aic.690330508>

Renardy, Y., & Renardy, M. (2002). PROST: a parabolic reconstruction of surface tension for the volume-of-fluid method. *Journal of Computational Physics*, 183(2), 400–421.

Roman, S., Soulaïne, C., AlSaud, M. A., Kovscek, A., & Tchelepi, H. (2016). Particle velocimetry analysis of immiscible two-phase flow in micromodels. *Advances in Water Resources*, 95, 199–211. <https://doi.org/10.1016/j.advwatres.2015.08.015>

ROOF JG. (1970). Snap-Off of Oil Droplets in Water- Wet Pores. *Soc Petrol Eng J*, 10(1), 85–90. <https://doi.org/10.2118/2504-pa>

Rossen, W. R. (2003). A critical review of Roof snap-off as a mechanism of steady-state foam generation in homogeneous porous media. *Colloids and Surfaces A: Physicochemical and Engineering Aspects*, 225(1–3), 1–24. [https://doi.org/10.1016/S0927-7757\(03\)00309-1](https://doi.org/10.1016/S0927-7757(03)00309-1)

Rossen, W. R. (2008). Comment on “Verification of Roof snap-off as a foam-generation mechanism in porous media at steady state.” *Colloids and Surfaces A: Physicochemical and Engineering Aspects*, 322(1–3), 261–269. <https://doi.org/10.1016/j.colsurfa.2008.02.034>

Singh, K., Bultreys, T., Raeini, A. Q., Shams, M., & Blunt, M. J. (2019). Imbibition in porous media : correlations of displacement events with pore-throat geometry and the identification of a new type of pore snap-off. *EarthArXiv*, (August), 1–12. <https://doi.org/10.31223/osf.io/62gfr>

Singh, Kamaljit, Menke, H., Andrew, M., Lin, Q., Rau, C., Blunt, M. J., & Bijeljic, B. (2017). Dynamics of snap-off and pore-filling events during two-phase fluid flow in permeable media. *Scientific Reports*, 7(1), 1–13. <https://doi.org/10.1038/s41598-017-05204-4>

Skauge, A., Solbakken, J., Ormehaug, P. A., & Aarra, M. G. (2020). Foam Generation, Propagation and

- Stability in Porous Medium. *Transport in Porous Media*, 131(1), 5–21.
<https://doi.org/10.1007/s11242-019-01250-w>
- Starnoni, M., & Pokrajac, D. (2018). Numerical study of the effects of contact angle and viscosity ratio on the dynamics of snap-off through porous media. *Advances in Water Resources*, 111(November 2017), 70–85. <https://doi.org/10.1016/j.advwatres.2017.10.030>
- Tan, Y. C., Ho, Y. L., & Lee, A. P. (2007). Droplet coalescence by geometrically mediated flow in microfluidic channels. *Microfluidics and Nanofluidics*, 3(4), 495–499.
<https://doi.org/10.1007/s10404-006-0136-1>
- Tanino, Y., & Blunt, M. J. (2012). Capillary trapping in sandstones and carbonates: Dependence on pore structure. *Water Resources Research*, 48(8), 1–13. <https://doi.org/10.1029/2011WR011712>
- Tiznado, J. A. Q., Fuentes, C., Sosa, E. G., & Chávez, C. (2018). Snap-off criteria for dynamic flow conditions in constricted circular capillaries. *Journal of Applied Fluid Mechanics*, 11(2), 447–457.
<https://doi.org/10.29252/jafm.11.02.27527>
- Valvatne, P. H., & Blunt, M. J. (2004). Predictive pore-scale modeling of two-phase flow in mixed wet media. *Water Resources Research*, 40(7), 1–21. <https://doi.org/10.1029/2003WR002627>
- Xie, C., Raeini, A. Q., Wang, Y., Blunt, M. J., & Wang, M. (2017). An improved pore-network model including viscous coupling effects using direct simulation by the lattice Boltzmann method. *Advances in Water Resources*, 100, 26–34. <https://doi.org/10.1016/j.advwatres.2016.11.017>
- Xu, K., Zhu, P., Huh, C., & Balhoff, M. T. (2015). Microfluidic Investigation of Nanoparticles Role in Mobilizing Trapped Oil Droplets in Porous Media. *Langmuir*, 31(51), 13673–13679.
<https://doi.org/10.1021/acs.langmuir.5b03733>
- Xu, K., Liang, T., Zhu, P., Qi, P., Lu, J., Huh, C., & Balhoff, M. (2017). A 2.5-D glass micromodel for investigation of multi-phase flow in porous media. *Lab on a Chip*, 17(4), 640–646.
<https://doi.org/10.1039/c6lc01476c>
- Xu, K., Zhu, P., Colon, T., Huh, C., & Balhoff, M. (2017). A microfluidic investigation of the synergistic effect of nanoparticles and surfactants in macro-emulsion-based enhanced oil recovery. *SPE Journal*, 22(2), 459–469. <https://doi.org/10.2118/179691-PA>